

Optical efficiency and gain dynamics of modelocked semiconductor disk lasers

C. G. E. ALFIERI,^{1,*} D. WALDBURGER,¹ S. M. LINK,¹ E. GINI,² M. GOLLING,¹ G. EISENSTEIN,³ AND U. KELLER¹

¹Department of Physics, Institute for Quantum Electronics, ETH Zurich, Auguste-Piccard-Hof 1, 8093 Zurich, Switzerland

²FIRST Center for Micro- and Nanoscience, ETH Zurich, 8093 Zurich, Switzerland

³Electrical Engineering Department and Russell Berrie Nanotechnology Institute, Technion Haifa 32000 Israel

*calfieri@phys.ethz.ch

Abstract: Compact optically pumped passively modelocked semiconductor disk lasers (SDLs) based on active quantum wells (QWs) such as vertical external-cavity surface-emitting lasers (VECSELs) or modelocked integrated external-cavity surface-emitting lasers (MIXSELs) are wavelength-versatile sources that offer a unique combination of gigahertz pulse repetition rates and short pulse durations. In this paper, we present record-short pulses of 184 fs from a gigahertz MIXSEL emitting at a center wavelength of 1048 nm. This result comes at the expense of low optical-to-optical pump efficiency (<1%) and average output power limited to 115 mW. We experimentally observe that shorter pulses significantly reduce the macroscopic gain saturation fluence and develop a QW model based on rate equations to reproduce the gain saturation behavior and quantitatively explain the VECSEL and MIXSEL modelocking performances. We identify spectral hole burning as the main cause of the reduced gain at shorter pulse durations, which in combination with the short lifetime of the excited carriers strongly reduces the optical pump efficiency. Our better understanding will help to address these limitations in future ultrafast SDL designs.

© 2017 Optical Society of America

OCIS codes: (140.3460) Lasers; (140.4050) Mode-locked lasers; (140.5960) Semiconductor lasers; (140.7090) Ultrafast lasers; (140.7270) Vertical emitting lasers.

References and links

- U. Keller and A. C. Tropper, "Passively modelocked surface-emitting semiconductor lasers," *Phys. Rep.* **429**(2), 67–120 (2006).
- B. W. Tilma, M. Mangold, C. A. Zaugg, S. M. Link, D. Waldburger, A. Klenner, A. S. Mayer, E. Gini, M. Golling, and U. Keller, "Recent advances in ultrafast semiconductor disk lasers," *Light Sci. Appl.* **4**(7), e310 (2015).
- M. Gaafar, A. Rahimi-Iman, K. A. Fedorova, W. Stoltz, E. U. Rafailov, and M. Koch, "Mode-locked semiconductor disk lasers," *Adv. Opt. Photonics* **8**(3), 370–400 (2016).
- S. Hoogland, S. Dhanjal, A. C. Tropper, J. S. Roberts, R. Haring, R. Paschotta, F. Morier-Genoud, and U. Keller, "Passively mode-locked diode-pumped surface-emitting semiconductor laser," *IEEE Photonics Technol. Lett.* **12**(9), 1135–1137 (2000).
- M. Kuznetsov, F. Hakimi, R. Sprague, and A. Mooradian, "High-power (>0.5-W CW) diode-pumped vertical-external-cavity surface-emitting semiconductor lasers with circular TEM00 beams," *IEEE Photonics Technol. Lett.* **9**(8), 1063–1065 (1997).
- S. H. Park, J. Kim, H. Jeon, T. Sakong, S. N. Lee, S. Chae, Y. Park, C. H. Jeong, G. Y. Yeom, and Y. H. Cho, "Room-temperature GaN vertical-cavity surface-emitting laser operation in an extended cavity scheme," *Appl. Phys. Lett.* **83**(11), 2121–2123 (2003).
- M. Guina, A. Härkönen, V.-M. Korpilähti, T. Leinonen, and S. Suomalainen, "Semiconductor Disk Lasers: Recent Advances in Generation of Yellow-Orange and Mid-IR Radiation," *Adv. Opt. Technol.* **2012**(19), 265010 (2012).
- R.-I. Arash, "Recent advances in VECSELs," *J. Optics-UK* **18**(9), 093003 (2016).
- B. Rudin, A. Rutz, M. Hoffmann, D. J. H. C. Maas, A.-R. Bellancourt, E. Gini, T. Südmeyer, and U. Keller, "Highly efficient optically pumped vertical-emitting semiconductor laser with more than 20 W average output power in a fundamental transverse mode," *Opt. Lett.* **33**(22), 2719–2721 (2008).

10. B. Heinen, T. L. Wang, M. Sparenberg, A. Weber, B. Kunert, J. Hader, S. W. Koch, J. V. Moloney, M. Koch, and W. Stolz, "106 W continuous-wave output power from vertical-external-cavity surface-emitting laser," *Electron. Lett.* **48**(9), 516–517 (2012).
11. U. Keller, K. J. Weingarten, F. X. Kärtner, D. Kopf, B. Braun, I. D. Jung, R. Fluck, C. Hönniger, N. Matuschek, and J. Aus der Au, "Semiconductor saturable absorber mirrors (SESAMs) for femtosecond to nanosecond pulse generation in solid-state lasers," *IEEE J. Sel. Top. Quantum Electron.* **2**(3), 435–453 (1996).
12. D. Waldburger, S. M. Link, M. Mangold, C. G. E. Alfieri, E. Gini, M. Golling, B. W. Tilma, and U. Keller, "High-power 100 fs semiconductor disk lasers," *Optica* **3**(8), 844–852 (2016).
13. D. J. H. C. Maas, A.-R. Bellancourt, B. Rudin, M. Golling, H. J. Unold, T. Südmeyer, and U. Keller, "Vertical integration of ultrafast semiconductor lasers," *Appl. Phys. B* **88**(4), 493–497 (2007).
14. B. Rudin, V. J. Wittwer, D. J. H. C. Maas, M. Hoffmann, O. D. Sieber, Y. Barbarin, M. Golling, T. Südmeyer, and U. Keller, "High-power MIXSEL: an integrated ultrafast semiconductor laser with 6.4 W average power," *Opt. Express* **18**(26), 27582–27588 (2010).
15. M. Mangold, M. Golling, E. Gini, B. W. Tilma, and U. Keller, "Sub-300-femtosecond operation from a MIXSEL," *Opt. Express* **23**(17), 22043–22059 (2015).
16. M. Mangold, C. A. Zaugg, S. M. Link, M. Golling, B. W. Tilma, and U. Keller, "Pulse repetition rate scaling from 5 to 100 GHz with a high-power semiconductor disk laser," *Opt. Express* **22**(5), 6099–6107 (2014).
17. S. M. Link, A. Klenner, M. Mangold, C. A. Zaugg, M. Golling, B. W. Tilma, and U. Keller, "Dual-comb modelocked laser," *Opt. Express* **23**(5), 5521–5531 (2015).
18. S. M. Link, D. J. H. C. Maas, D. Waldburger, and U. Keller, Submitted to *Science* (January 2017).
19. O. D. Sieber, M. Hoffmann, V. J. Wittwer, M. Mangold, M. Golling, B. W. Tilma, T. Südmeyer, and U. Keller, "Experimentally verified pulse formation model for high-power femtosecond VECSELs," *Appl. Phys. B* **113**(1), 133–145 (2013).
20. K. Sugioka and Y. Cheng, "Ultrafast lasers—reliable tools for advanced materials processing," *Light Sci. Appl.* **3**(4), e149 (2014).
21. R. Aviles-Espinosa, G. Filippidis, C. Hamilton, G. Malcolm, K. J. Weingarten, T. Südmeyer, Y. Barbarin, U. Keller, S. I. C. O. Santos, D. Artigas, and P. Loza-Alvarez, "Compact ultrafast semiconductor disk laser: targeting GFP based nonlinear applications in living organisms," *Biomed. Opt. Express* **2**(4), 739–747 (2011).
22. C. A. Zaugg, A. Klenner, M. Mangold, A. S. Mayer, S. M. Link, F. Emaury, M. Golling, E. Gini, C. J. Saraceno, B. W. Tilma, and U. Keller, "Gigahertz self-referencable frequency comb from a semiconductor disk laser," *Opt. Express* **22**(13), 16445–16455 (2014).
23. A. H. Quarterman, L. E. Hooper, P. J. Mosley, and K. G. Wilcox, "Gigahertz pulse source by compression of mode-locked VECSEL pulses coherently broadened in the normal dispersion regime," *Opt. Express* **22**(10), 12096–12101 (2014).
24. H. R. Telle, G. Steinmeyer, A. E. Dunlop, J. Stenger, D. H. Sutter, and U. Keller, "Carrier-envelope offset phase control: A novel concept for absolute optical frequency measurement and ultrashort pulse generation," *Appl. Phys. B* **69**(4), 327–332 (1999).
25. A. Klenner, A. S. Mayer, A. R. Johnson, K. Luke, M. R. E. Lamont, Y. Okawachi, M. Lipson, A. L. Gaeta, and U. Keller, "Gigahertz frequency comb offset stabilization based on supercontinuum generation in silicon nitride waveguides," *Opt. Express* **24**(10), 11043–11053 (2016).
26. A. S. Mayer, A. Klenner, A. R. Johnson, K. Luke, M. R. E. Lamont, Y. Okawachi, M. Lipson, A. L. Gaeta, and U. Keller, "Frequency comb offset detection using supercontinuum generation in silicon nitride waveguides," *Opt. Express* **23**(12), 15440–15451 (2015).
27. J. V. Moloney, I. Kilen, A. Bäumner, M. Scheller, and S. W. Koch, "Nonequilibrium and thermal effects in mode-locked VECSELs," *Opt. Express* **22**(6), 6422–6427 (2014).
28. I. Kilen, J. Hader, J. V. Moloney, and S. W. Koch, "Ultrafast nonequilibrium carrier dynamics in semiconductor laser mode locking," *Optica* **1**(4), 192–197 (2014).
29. J. Hader, M. Scheller, A. Laurain, I. Kilen, C. Baker, J. V. Moloney, and S. W. Koch, "Ultrafast non-equilibrium carrier dynamics in semiconductor laser mode-locking," *Semicond. Sci. Technol.* **32**(1), 013002 (2017).
30. I. Kilen, S. W. Koch, J. Hader, and J. V. Moloney, "Fully microscopic modeling of mode locking in microcavity lasers," *J. Opt. Soc. Am. B* **33**(1), 75–80 (2016).
31. N. Tessler and G. Eisenstein, "Modelling carrier dynamics and small-signal modulation response in quantum-well lasers," *Opt. Quantum Electron.* **26**(7), S767–S787 (1994).
32. N. Tessler and G. Eisenstein, "On carrier injection and gain dynamics in quantum well lasers," *IEEE J. Quantum Electron.* **29**(6), 1586–1595 (1993).
33. H. Dery, B. Tromborg, and G. Eisenstein, "Carrier-carrier relaxation kinetics in quantum well semiconductor structures with nonparabolic energy bands," *Phys. Rev. B* **68**(16), 165323 (2003).
34. C. G. E. Alfieri, A. Diebold, F. Emaury, E. Gini, C. J. Saraceno, and U. Keller, "Improved SESAMs for femtosecond pulse generation approaching the kW average power regime," *Opt. Express* **24**(24), 27587–27599 (2016).
35. T. R. Schibli, E. R. Thoen, F. X. Kärtner, and E. P. Ippen, "Suppression of Q-switched mode locking and break-up into multiple pulses by inverse saturable absorption," *Appl. Phys. B* **70**(S1 Suppl.), S41–S49 (2000).
36. R. Trebino, K. W. DeLong, D. N. Fittinghoff, J. N. Sweetser, M. A. Krumbügel, B. Richman, and D. J. Kane, "Measuring ultrashort laser pulses in the time-frequency domain using frequency-resolved optical gating," *Rev. Sci. Instrum.* **68**(9), 3277–3295 (1997).

37. N. Tessler, R. Nagar, and G. Eisenstein, "Structure dependent modulation responses in quantum-well lasers," *IEEE J. Quantum Electron.* **28**(10), 2242–2250 (1992).
38. H. Toktamiş, B. Gönül, and M. Oduncuoğlu, "Comparative study of the band-offset ratio of conventionally strained and strain-compensated InGaAs/GaAs QW lasers," *Physica E* **24**(3–4), 183–186 (2004).
39. S. T. Cundiff, A. Knorr, J. Feldmann, S. W. Koch, E. O. Göbel, and H. Nickel, "Rabi flopping in semiconductors," *Phys. Rev. Lett.* **73**(8), 1178–1181 (1994).
40. J. Hader, J. V. Moloney, and S. W. Koch, "Microscopic analysis of non-equilibrium dynamics in the semiconductor-laser gain medium," *Appl. Phys. Lett.* **104**(15), 151111 (2014).
41. O. Karni, A. K. Mishra, G. Eisenstein, V. Ivanov, and J. P. Reithmaier, "Coherent control in room-temperature quantum dot semiconductor optical amplifiers using shaped pulses," *Optica* **3**(6), 570–576 (2016).
42. A. P. Ongstad, D. J. Gallant, and G. C. Dente, "Carrier lifetime saturation in InGaAs single quantum wells," *Appl. Phys. Lett.* **66**(20), 2730–2732 (1995).
43. C. K. Sun, B. Golubovic, H. K. Choi, C. A. Wang, and J. G. Fujimoto, "Femtosecond investigations of spectral hole burning in semiconductor lasers," *Appl. Phys. Lett.* **66**(13), 1650–1652 (1995).
44. M. Asada, "Intraband relaxation time in quantum-well lasers," *IEEE J. Quantum Electron.* **25**(9), 2019–2026 (1989).
45. C. Baker, M. Scheller, S. W. Koch, A. R. Perez, W. Stoltz, R. Jason Jones, and J. V. Moloney, "In situ probing of mode-locked vertical-external-cavity-surface-emitting lasers," *Opt. Lett.* **40**(23), 5459–5462 (2015).
46. M. Mangold, V. J. Wittwer, O. D. Sieber, M. Hoffmann, I. L. Krestnikov, D. A. Livshits, M. Golling, T. Südmeyer, and U. Keller, "VECSEL gain characterization," *Opt. Express* **20**(4), 4136–4148 (2012).
47. M. Butkus, E. A. Viktorov, T. Erneux, C. J. Hamilton, G. Maker, G. P. A. Malcolm, and E. U. Rafailov, "85.7 MHz repetition rate mode-locked semiconductor disk laser: fundamental and soliton bound states," *Opt. Express* **21**(21), 25526–25531 (2013).
48. C. A. Zaugg, A. Klenner, O. D. Sieber, M. Golling, B. W. Tilma, and U. Keller, "Sub-100 MHz Passively Modelocked VECSEL," in *CLEO: 2013, OSA Technical Digest (online)* (Optical Society of America, 2013), CW1G.6.
49. A. Klenner, M. Golling, and U. Keller, "High peak power gigahertz Yb:CALGO laser," *Opt. Express* **22**(10), 11884–11891 (2014).
50. C. G. E. Alfieri, D. Waldburger, S. M. Link, E. Gini, M. Golling, B. W. Tilma, M. Mangold, and U. Keller, "Recent progress in high power ultrafast MIXSELs," in *Proc. SPIE* (2016), p. 973407.

1. Introduction

We have obtained systematic improvements of ultrafast optically pumped semiconductor disk lasers (SDLs) [1] during the last decade [2, 3] since the first demonstration in 2000 [4]. Semiconductor bandgap engineering of optically pumped vertical-external cavity surface-emitting lasers (VECSELs) [5] provides selected lasing wavelengths optimized for specific applications. To date, modelocked operation has been demonstrated from the UV up to 2 μm and in continuous wave (cw) operation even up to the mid-IR (i.e. up to 5 μm) [5–8]. The highest output power is achieved with InGaAs quantum well gain materials emitting at a center wavelength of around 1 μm . In continuous wave (cw) operation, InGaAs based VECSELs demonstrated up to 20 W of output power in a fundamental Gaussian mode [9] and 106 W in multimode [10]. For modelocked SDLs, optically pumped VECSELs passively modelocked with semiconductor saturable absorber mirrors (SESAMs) [11] provide the shortest pulses of 96 fs with 100 mW of average output power in fundamental modelocking (i.e. one single pulse per roundtrip) [12]. A more compact ultrafast SDL is obtained with the modelocked integrated external-cavity surface-emitting laser (MIXSEL) [13], where the SESAM's saturable absorber is vertically integrated in the VECSEL gain structure. This results in a simple linear cavity with just 2 end mirrors represented by the semiconductor MIXSEL chip and the curved output coupler [Fig. 1(c)]. MIXSELs have demonstrated the highest output power of any modelocked SDLs, with 6.4 W in 28 ps pulses [14] and have reached pulse durations as short as 253 fs so far [15]. Furthermore the simple linear cavity enabled record-high pulse repetition rates up to 100 GHz [16] and dual-comb modelocking with excellent stability [17, 18]. Following the design guidelines explained in [19], we present here further performance improvement with a MIXSEL generating pulses as short as 184 fs at a pulse repetition rate of 4.33 GHz. The average output power was limited to 115 mW, corresponding to a peak power of 127 W, and the optical-to-optical pump efficiency was 0.65%.

For cw InGaAs QW-VECSELs, optical-to-optical pump efficiencies as high as 45% in multimode output [10] and 43.2% in fundamental Gaussian mode output [9] are reported. For femtosecond pulse durations, however, the efficiency is typically reduced to below 1% [12, 15]. Furthermore, for shorter pulse durations we typically observe a decreased pulse energy and therefore a limited average output power. This trade-off in both the pump efficiency and average output power with shorter pulse durations sets serious restrictions for applications that require a combination of short femtosecond pulses and high peak power to drive nonlinear optical processes such as frequency doubling for material processing [20], multiphoton microscopy [21] and supercontinuum generation for metrology and frequency comb applications [22, 23]. For this reason we recently focused our efforts to relax the hard peak power requirements of sub-100-femtosecond pulses necessary to detect and stabilize the carrier-envelope-offset (CEO) frequency in a self-referenced f-to-2f interferometry scheme [24] for frequency comb stabilization thanks to promising results with Si₃N₄ waveguides for supercontinuum generation [25, 26].

In this paper, we want to develop a simple model that explains the observed trade-off between short pulse duration and pump efficiency. Recently, simulations relying on the development of fully microscopic many-body QW models based on Maxwell semiconductor Bloch equations [27–29] revealed that amplification of short pulses significantly decreases the carrier population in the inverted distribution creating kinetic holes. Under strong pumping conditions we have a reservoir of unused carriers outside of the spectral pulse domain that can seed additional pulses which destabilize fundamental modelocking. Such ab-initio models offer a deep understanding for modelocked QW-VECSELs, but rely on a considerable computational effort and were up to now calculated only for resonant periodic gain structures [30]. Furthermore, several important quantities that cannot be theoretically predicted like inevitable growth inaccuracies, inhomogeneity of the layer thicknesses and influence of defect-recombination on the carrier lifetime limit the quantitative prediction capability of fully microscopic models for real structures, forcing a final adjustment of the theoretical results to macroscopic experimental data to obtain a proper quantitative description of the modelocking process.

Following the more phenomenological approach we introduced in [19] to simulate pulse formation processes in ultrafast SDLs, we expand here our efforts with a simplified QW gain model based on single carrier type rate equations (REs) [31, 32]. Our model provides a better understanding on various limitations of current SDLs and can reproduce the experimental values of output power and pump efficiency for different MIXSELs and VECSELs [12, 15]. As a key advantage of the introduced simplifications, most physical input parameters necessary for simulation can be directly measured.

We distinguish three time scales involved in SDL carrier dynamics [29]: a nanosecond time scale for the diffusion process of the optically pumped electrons and holes into the QW gain region, a 100-ps time scale for interband spontaneous recombination and finally a time scale in the hundreds of femtoseconds for intraband scattering phenomena. Through pump-probe and gain/absorption saturation measurements of our VECSELs, MIXSELs and SESAMs, we directly obtain or fit the model input parameters and arrive at a quantitative explanation for the limited pulse fluence that is experimentally observed during modelocking.

Consistently with [33], we confirm in this paper that spectral hole burning is responsible for a lower gain saturation fluence with shorter pulse durations and is currently preventing power scaling in the sub-200-fs regime. In addition we can demonstrate that two-photon absorption (TPA) does not yet set a significant limitation for the output power even though TPA becomes stronger with shorter pulses [34, 35]. In contrast, we confirm that a short carrier lifetime in the conduction band in the order of 100 ps strongly reduces the optical-to-optical pump efficiency.

The paper is structured as follows. In section 2 we describe the recent modelocking improvements for our MIXSEL generating 184-fs pulses; section 3 focuses on the description

of the RE QW model, while sections 4 and 5 show that the measured pulse-energy-dependent gain dynamics and gain saturation can be reproduced by this model. In section 6 and 7 we use this model to simulate and explain the modelocking performances and pump efficiencies of the SESAM modelocked VECSEL generating 100-fs pulses, as described in more details in [12], and of the 184-fs MIXSEL result.

2. Experimental MIXSEL modelocking results

2.1 MIXSEL design and fabrication

In Fig. 1(a) we show the semiconductor epitaxial layer stack of the MIXSEL chip which is the same as described in [15]. The structure is designed for an operation wavelength around 1040-1050 nm. Going from the bottom to the top, the MIXSEL chip consists of a bottom 24-pair AlAs/GaAs distributed Bragg reflector (DBR) which forms a high reflective mirror for the lasing wavelength, followed by an absorber section with a single 11-nm thick $\text{In}_{0.2}\text{Ga}_{0.8}\text{As}$ W and a 9.5 pair $\text{Al}_{0.15}\text{Ga}_{0.85}\text{As}/\text{AlAs}$ DBR designed to reflect the pump wavelength and prevent bleaching of the absorber due to the residual pump light. This is followed by an active region with 10 $\text{In}_{0.19}\text{Ga}_{0.81}\text{As}$ QWs of 9 nm thickness embedded in GaAs barriers. The compressive strain of the gain QWs is balanced by tensile strained layers of $\text{GaAs}_{0.94}\text{P}_{0.06}$.

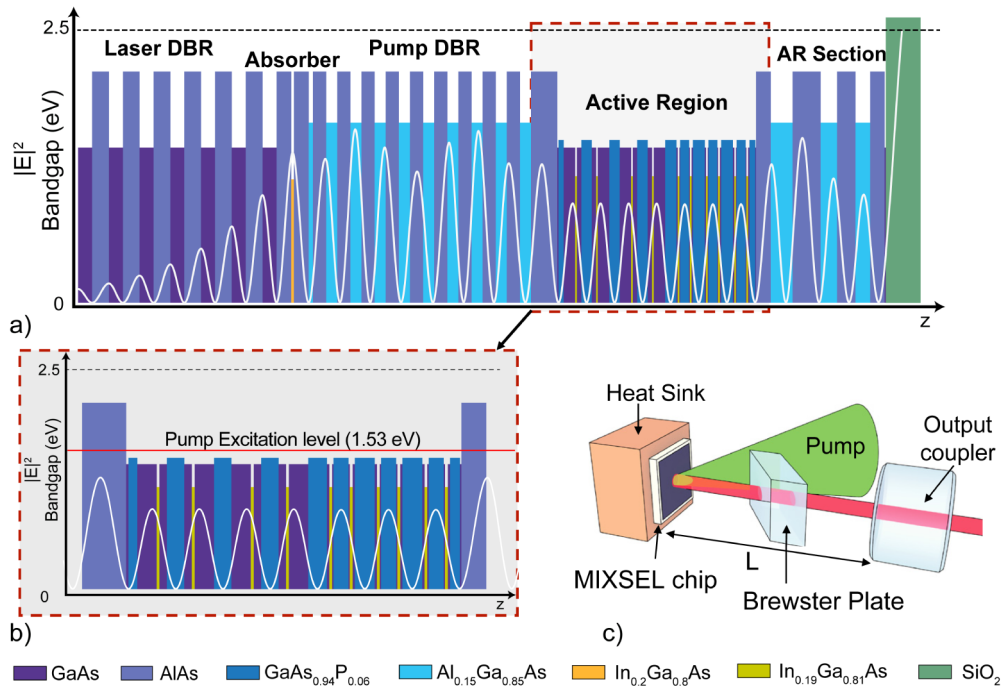


Fig. 1. Modelocked integrated external-cavity surface-emitting laser (MIXSEL) which generates pulses as short as 184 fs: (a) Layer stack of the semiconductor MIXSEL chip. The standing electric intensity wave pattern is normalized to 4 outside of the structure. (b) Zoom into the active region of the layer stack: AlAs barriers with a higher bandgap energy define the active region and confine the carriers generated through optical pump absorption in the GaAs and $\text{GaAs}_{0.94}\text{P}_{0.06}$ layers. (c) Simple linear MIXSEL cavity. The semiconductor MIXSEL chip forms one cavity end mirror and the output coupler (OC) the other. The OC has a 350-mm radius of curvature (ROC) and a transmission T_{OC} of 0.44%. An intracavity Brewster plate is used for polarization selection. The MIXSEL chip is pumped with a high-power diode laser array under a 45° angle. For a pulse repetition rate of ≈ 4.3 GHz in fundamental modelocking, we use a cavity length L of ≈ 3.5 cm.

Passive modelocking is achieved following the design guidelines in [19]. The average electric field intensity enhancement factor at the QW positions was reduced to 0.65 (normalized to 4 out of a 100% reflective mirror) to increase the gain saturation fluence and flattened with variations below 10% over a range of ± 20 nm around the center wavelength to support broadband operation. A numerically optimized antireflection (AR) section with seven alternating layers of $\text{Al}_{0.15}\text{Ga}_{0.85}\text{As}$ and AlAs followed by a single fused silica (FS) layer finalizes the structure. This last AR section minimizes the pump reflection and provides a close to constant group delay dispersion (GDD) in a range of ± 200 fs² over a 40-nm bandwidth around the lasing wavelength.

As described in [15], the semiconductor layer structure was grown in the FIRST lab at ETH Zurich. The growth was in reverse order for subsequent flip-chip bonding on a diamond heat spreader. The etch-stop layer, the AR section and the active region were grown in a metalorganic vapor phase epitaxy (MOVPE) machine to benefit from the P-based strain compensation layers. The two DBRs and the saturable absorber were grown using a molecular beam epitaxy (MBE) system to take advantage of the currently lower saturation fluence achieved with saturable absorbers grown by MBE. The single fused silica layer was deposited by plasma enhanced chemical vapor deposition (PECVD).

Compared to the structure used in [15], we improved the precision of the PECVD deposition process and adapted the fused silica thickness to partially compensate small deviations from design observed in the epitaxial structure due to growth errors. This provided a better dispersion management and enabled generation of shorter pulses.

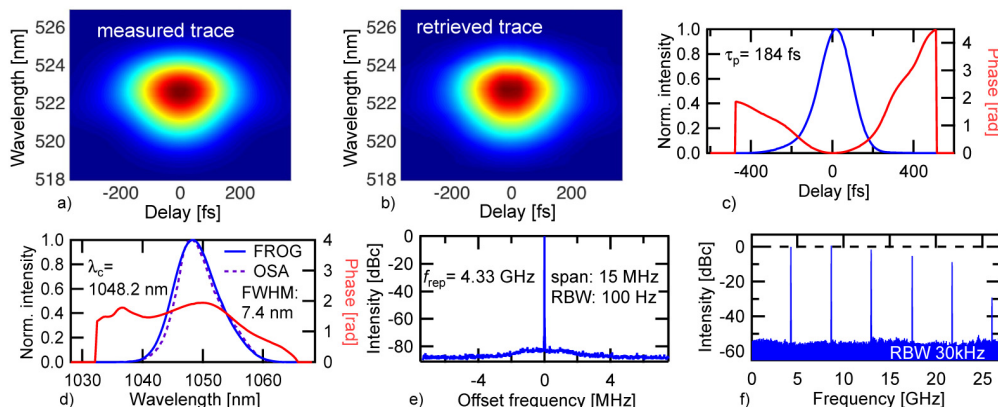


Fig. 2. Modelocking results of the 184-fs MIXSEL: (a) Measured SHG-FROG spectrogram. (b) Retrieved FROG spectrogram (error 0.0011). (c) Retrieved temporal profile and spectral phase. (d) Retrieved spectral intensity and spectral phase overlapped with the measured optical spectrum centered at 1048 nm with a FWHM of 7.4 nm. (e) Microwave spectrum centered at the fundamental repetition rate of 4.33 GHz with a span of 15 MHz and 100 Hz RBW. (f) Microwave spectrum over a larger frequency span with a RBW of 30 kHz. The power decrease for the higher harmonics is a consequence of the limited bandwidth of the photodetector.

2.2 Modelocking performance

The MIXSEL chip was mounted on a copper heatsink and temperature stabilized at 9°C. A linear laser cavity is obtained with the MIXSEL chip as one end mirror and a curved output coupler (OC) as the other [Fig. 1(c)]. The OC has a 350-mm radius of curvature (ROC) and a transmission T_{OC} of 0.44%. The cavity length was set to 34.6 mm, corresponding to a pulse repetition rate of 4.33 GHz in fundamental modelocking operation. The MIXSEL chip was pumped under an angle of 45° with a commercial multimode 808 nm fiber coupled diode array. To ensure single transverse mode operation, the laser spot size on the MIXSEL was set to a 184-μm radius, slightly larger than the circular pump spot size of a 180-μm radius on the MIXSEL chip. A 1-mm thick wedged fused silica plate was inserted into the cavity at

Brewster angle to obtain a single linear polarization output. With the incident pump power increased to 17.6 W, self-starting stable modelocking operation was achieved at an average output power of 115 mW, corresponding to a pulse peak power of 127 W. A detailed pulse characterization carried out with second harmonic generation frequency resolved optical gating (SHG FROG) revealed a duration of 184 fs, which represents the shortest pulse duration ever achieved with the MIXSEL technology. Good agreement between the measured and the retrieved trace is visible in Figs. 2(a) and 2(b), with a reconstruction error of 0.0011 [36]. The pulse spectrum, measured with both FROG and optical spectrum analyzer, shows a center wavelength of 1048 nm and a full width at half maximum (FWHM) bandwidth of 7.4 nm, corresponding to 1.15 times the time-bandwidth product for an ideal transform-limited sech²-shaped pulse.

The detected microwave spectrum was measured with a 22-GHz photodetector without additional amplification. The fundamental pulse repetition rate of 4.33 GHz measured in a 15-MHz span with a narrow resolution bandwidth (RBW) of 100 Hz shows a high signal-to-noise ratio of more than 80 dB indicating fundamental modelocking operation [Fig. 2(e)]. In addition, we show several harmonics of the fundamental pulse repetition rate in a large-span measurement taken with a RBW of 30 kHz [Fig. 2(f)]. The reduced power in the higher harmonics results from the limited detection bandwidth.

2.3 Current limitations

With this new modelocking result we demonstrate for the first time pulse durations below 250 fs with a MIXSEL. This improvement validates our design guidelines as presented in [19]. However, it unfortunately confirms again the significant trade-off in output power and pump efficiency with shorter pulse durations. In particular, for our 184-fs result the optical-to-optical pump efficiency does not exceed the low value of 0.65%. Moreover, the intracavity pulse fluence on the MIXSEL device during modelocked operation was limited to 5.8 $\mu\text{J}/\text{cm}^2$ and the OC transmission to 0.44%.

To better understand the physical origin for this trade-off, we develop a QW rate equation model that can benefit from our measured input parameters.

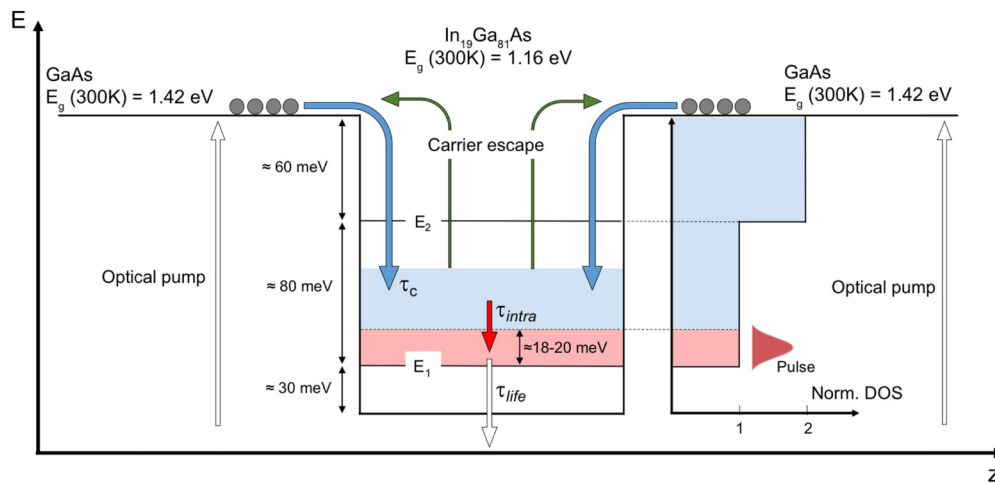


Fig. 3. Ambipolar quantum well (QW) model. Carriers diffuse from the optically pumped GaAs barriers into the QW with a time constant τ_c , then relax to the bottom of the band with an intraband time constant τ_{intra} . Finally, they spontaneously recombine with a time constant τ_{life} . The normalized density of states (DOS) is depicted on the right side of the QW. N_1 corresponds to the region interested by stimulated emission and spontaneous recombination; N_2 acts as a carrier reservoir

3. QW rate equation model

We have employed a rate equation model for the strain compensated $\text{In}_{0.19}\text{Ga}_{0.81}\text{As}$ gain QWs embedded in GaAs barriers used in both a MIXSEL (Fig. 1) and a SESAM modelocked VECSEL presented in [12]. Our goal is to obtain a precise quantitative description of the laser performance and a better understanding of their limitations. It is therefore important to minimize the number of input parameters for our model which cannot be measured directly. This leads to the introduction of several assumptions and simplifications that are explained as follows.

- Flat-band approximation. No external electric field is applied and no net current is flowing in the undoped laser structure. Carriers diffuse in the optically pumped GaAs barriers and are captured in the QW. An internal electric field is always formed due to a Coulomb interaction between electrons and holes that diffuse with different diffusion coefficients. The electric field causes a nonuniform carrier distribution with a larger carrier density close to the P side of the junction [32]. However, in the present structure the effect is minor and the carrier transport can be modeled as an ambipolar process [37].
- Band structure of the QW. The band-offset between GaAs barriers and strain compensated $\text{In}_{0.19}\text{Ga}_{0.81}\text{As}$ QW is 255 meV at 300 K. Since the temperature dependence of the energy bandgap is similar for the two materials, we consider the band-offset constant and keep the same value for the laser operation temperature in the active region, which is assumed to be 370-400 K. We define the zero energy in correspondence of the bottom of the bulk $\text{In}_{0.19}\text{Ga}_{0.81}\text{As}$ conduction band and estimate a band-offset ratio of 0.67 [38], meaning that the GaAs barriers are 170 meV high. The confinement effects shift the first energy sub-band at ≈ 30 meV and the second at ≈ 110 meV respectively (Fig. 3).
- Capture and escape rates. The different QWs in the laser structure are separated by several tens of nanometers, making electron coupling (by tunneling) between them negligible. We define a constant net carrier capture rate into the QW ($1/\tau_c$) which is determined by carrier diffusion through the pumped barriers and the relaxation rate into the QW itself. This net rate considers also the escape rate, which is related, at equilibrium to the capture rate by the principle of detailed balance. The ratio of escape-to-capture rate is assumed to remain constant under steady-state modelocking conditions. This is verified by the fact that under normal operation, the QW is not completely filled and $2 - 3 k_B T$ separate the last occupied QW state and the barriers which ensures that the escape probability is unperturbed.
- Two-level approximation. We divide the continuum of the energy states in the QW into two spectral regions. We define an interaction region which corresponds to the lowest 18-20 meV of the conduction band (sufficient to support the full spectral content of a ≈ 100 fs pulse at 1 μm), and call N_1 the corresponding carrier density (Fig. 3). We make the assumption that spontaneous and stimulated emission events take place in this region independently of the spectral bandwidth of the incoming pulse, which is reasonable for pulses longer than the typical Rabi oscillation time scale (≈ 50 fs [39–41]). The population at higher energies, referred to as N_2 acts as a carrier reservoir.
- Carrier dynamics. We assume that carriers diffuse from the barriers into N_2 with a capture time constant τ_c in the nanosecond regime [42]. The relaxation to N_1 (i.e. the bottom of the band) takes place with a relative slow intraband time constant τ_{intra} .

in the hundreds of femtoseconds [43]. Carriers in N_1 decay through spontaneous recombination with a time constant τ_{life} in the hundreds of picoseconds. The local internal carrier re-distributions inside the single regions N_1 and N_2 are dominated by highly efficient intraband scattering processes involving small energy transfers with characteristic times in the tens of femtosecond range [40, 44], significantly shorter than the considered pulse durations. They are therefore assumed to be instantaneous.

- Fermi-Dirac distribution. The maximum occupancy in N_1 at equilibrium is governed by a Fermi-Dirac probability distribution and is therefore related to the total carrier density of the QW. While lasers are naturally not in real equilibrium, this approximation is commonly used in ambipolar models and works well.

These assumptions and approximations lead us to the following rate equations:

$$\frac{\partial N_1}{\partial t} = -\frac{N_1(t) - N'_{10}(t)}{\tau_{intra}} \cdot \frac{N_2(t)}{N_{20}} - \frac{N_1(t)}{\tau_{life}} - \Gamma_{gain} \cdot Pulse(t, F_p, \tau_p, \tau_0) \quad (1)$$

$$\frac{\partial N_2}{\partial t} = -\frac{N_2(t) - N_{20}(t)}{\tau_c} + \frac{N_1(t) - N'_{10}(t)}{\tau_{intra}} \cdot \frac{N_2(t)}{N_{20}} \quad (2)$$

where Γ_{gain} is the stimulated emission coefficient that couples the carriers in N_1 with the modelocked sech²-pulse interacting with the gain chip at τ_0 with a fluence F_p and a pulse duration τ_p . $N'_{10}(t)$ is given by:

$$N'_{10}(t) = \frac{N_{10}}{1 + \exp\left(\frac{E_0 - E_F(t)}{k_b T}\right)} \quad (3)$$

where N_{10} is the total amount of states in the N_1 region and E_0 is the average carrier energy (i.e. $\approx 9-10$ meV); $E_F(t)$ is the Fermi energy which depends on the total carrier density of the QW. Normalization of the density of states (DOS) (Fig. 3), leads to $E_F(t) = N_1(t) + N_2(t)$ until the second sub-band is reached. Defining ΔE as the energy difference between the two confined sub-bands, we obtain after the second sub-band: $E_F(t) = \frac{1}{2} \cdot (N_1(t) + N_2(t) + \Delta E)$.

In order to reproduce all the elements of a SDL cavity, we need to introduce an additional rate equation for the saturable absorber. We describe the population dynamics in the SESAM QW as follows:

$$\frac{\partial N_{abs}}{\partial t} = -\frac{N_{abs}(t)}{\tau_{abs}} + \Gamma_{abs} \cdot [1 - N_{abs}(t)] \cdot Pulse(t, K \cdot F_p, \tau_p, \tau_0) \quad (4)$$

where τ_{abs} is the SESAM recovery time defined by the recovery time of the reflectivity to the 1/e – value of its maximum saturation. Γ_{abs} represents the absorption rate related to the saturation fluence and K is the ratio between the fluence on the SESAM and the fluence on the gain chip ($K = 1$ in a MIXSEL with the same intensity enhancement in absorber and gain, assuming obviously the same laser spot size and the equal number of passages per roundtrip on gain and absorber).

Assuming the gain proportional to N_1 , we define the reflectivity experienced by a modelocked pulse after a full roundtrip time T in a straight MIXSEL cavity:

$$R_{\text{MIXSEL}}(F_p, \tau_p) = \frac{\int_0^T \text{Pulse}(t, F_p, \tau_p, \tau_0) \cdot \{1 + \sigma \cdot N_1(t) - \Delta R \cdot [1 - N_{\text{abs}}(t)] - \Delta R_{\text{ns}}\} \cdot dt}{\int_0^T \text{Pulse}(t, F_p, \tau_p, \tau_0) \cdot dt} \cdot e^{-\frac{F_p}{F_2(\tau_p)}} \quad (5)$$

where ΔR is the absorber modulation depth, ΔR_{ns} represents the nonsaturable losses of the structure, $F_2(\tau_p)$ is the TPA coefficient defined as in [34] and σ is:

$$\sigma = \frac{g_{ss}}{N_1(\infty)} \quad (6)$$

With g_{ss} being the measurable small signal gain and $N_1(\infty)$ the asymptotic value of N_1 obtained through (1) and (2) with no incoming pulse. If we take into account the double pass in the gain chip and the different laser spot sizes on VECSEL and SESAM, the roundtrip reflectivity is calculated for a VECSEL V-shaped cavity:

$$R_{\text{VECSEL}}(F_p, \tau_p) = \frac{\int_0^T \text{Pulse}(t, F_p, \tau_p, \tau_0) \cdot \{1 + 2\sigma \cdot N_1(t) - \Delta R \cdot [1 - N_{\text{abs}}(t)] - 2\Delta R_{\text{ns,VECSEL}} - \Delta R_{\text{ns,SESAM}}\} \cdot dt}{\int_0^T \text{Pulse}(t, F_p, \tau_p, \tau_0) \cdot dt} \cdot e^{-\frac{2F_p}{F_{2,\text{VECSEL}}(\tau_p)} - \frac{K \cdot F_p}{F_{2,\text{SESAM}}(\tau_p)}} \quad (7)$$

We expect small pulse variations during a single roundtrip during steady-state modelocking and therefore the same pulse reaches the VECSEL twice and the SESAM once per cavity roundtrip.

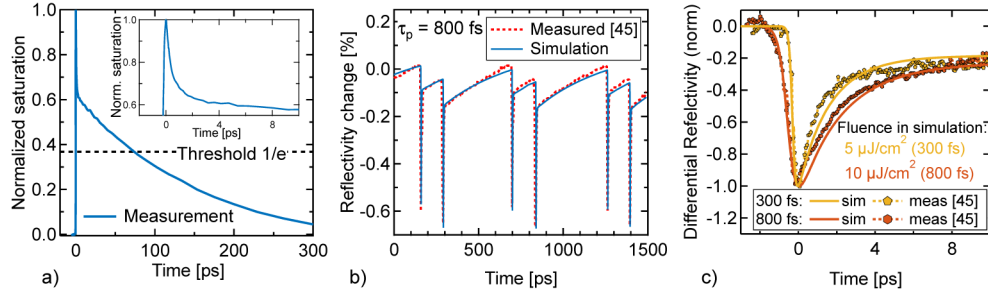


Fig. 4. (a) Saturation recovery measurement for a single $\text{In}_{0.19}\text{Ga}_{0.81}\text{As}$ QW. Inset: zoom into the initial fast recovery. (b) Gain dynamics of a modelocked VECSEL on a multi-roundtrip time scale. The gain chip folds a V-shaped cavity with unbalanced arm lengths. The strong drops in reflectivity correspond to the pulse arrival times on the gain chip. Our simulation is compared to measurements performed in [45]. (c) VECSEL fast gain recovery for two different pulse durations. The simulation is in good agreement with the measurements of [45].

4. Measurement and fit for the model input parameters

We fitted the RE model to experimental data in order to quantitatively reconstruct the gain dynamics and obtain values for the three time constants τ_c , τ_{intra} , τ_{lifc} as well as for the

stimulated emission coefficient Γ_{gain} . To directly obtain a value range for τ_{intra} and τ_{life} , we performed pump-probe measurements on a structure consisting of a DBR on top of which we placed a single $In_{0.19}Ga_{0.81}As$ QW, grown by MOVPE with the same growth parameters used for the active QWs of [12, 15] and for the 184-fs MIXSEL.

We used a standard degenerate pump-probe setup with a tunable Ti:sapphire laser generating 100-fs pulses (stretched to 130 fs at the sample position) at 80 MHz with an average power of 900 mW. The center wavelength was adjusted to the photoluminescence peak of the QW at room temperature (1020 nm). During the pump-probe measurement the structure was not cw pumped with 808-nm diode. The measurement revealed a saturation recovery with a fast temporal component of \approx 300-400 fs followed by a slow component of 130-140 ps [Fig. 4(a)]. These correspond to the value ranges used in the following for τ_{intra} and τ_{life} respectively.

Recently, *in situ* measurements of gain dynamics during modelocking operation have been shown in [45] for two VECSELs generating 300 fs and 800 fs pulses (these samples will be called hereon 300-fs VECSEL and 800-fs VECSEL). The fit of these experimental curves allowed us to extract values for τ_c and for Γ_{gain} (listed in Table 1). With all the parameters implemented in the RE model, the curves presented in [45] are well reproduced for both the 300-fs VECSEL and 800-fs VECSEL result [Figs. 4(b) and 4(c)].

5. Gain saturation

To verify the effect of pulse duration on gain saturation, we measured the pulse-fluence-dependent reflectivity of a diode pumped VECSEL probing the sample with different pulse durations but keeping the probe spectrum unchanged. To achieve a better signal-to-noise ratio in gain measurements, we designed for this experiment a high-gain, 10-QW, strain compensated VECSEL with relatively high average field intensity enhancement factor of 0.7 at the QW positions (at 1020 nm). This VECSEL chip (that we will call the 672-fs VECSEL) delivered up to 10 W of output power in cw operation and 700 mW of modelocked average output power with 672-fs pulses at 1022 nm.

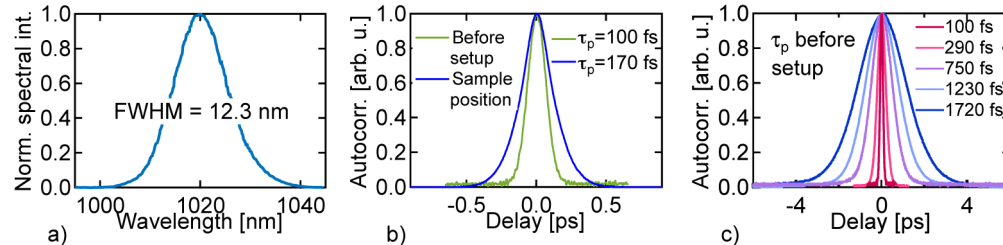


Fig. 5. Modelocking characterization of the Ti:sapphire laser used to probe the gain saturation of SDLs. (a) Measured optical spectrum centered at 1020 nm with FWHM bandwidth of 12.3 nm. (b) Autocorrelation trace directly at the laser output and at the sample position: the setup adds \approx 5000 fs² of positive GDD. (c) Autocorrelation trace (measured before setup) of the stretched pulses used to probe the gain.

We probed 672-fs VECSEL chip with the same Ti:sapphire laser previously described for the pump-probe measurements; the center wavelength was adjusted to 1020 nm and with a measured FWHM bandwidth of 12.3 nm [Fig. 5(a)].

To accurately measure the VECSEL reflectivity, we used a setup similar to [46]. The setup adds about 5000 fs² of group delay dispersion (GDD), therefore stretching the initial 100-fs pulse to 170 fs [Fig. 5(b)]. We test different pulse durations by stretching the pulses with 1, 3, 5, and 7 passages through a 9-cm block of SF-10 glass, adding roughly 9000 fs² of GDD per passage. As shown in Fig. 5(c), we obtained a maximum pulse duration of 1.72 ps before the setup, corresponding to 1.89 ps on the sample. The VECSEL was mounted on a

temperature stabilized heat sink and pumped with a cw multimode 808-nm diode laser array. During the measurement, we set the heat sink temperature to 5°C and the pump intensity to 57 kW/cm².

The measured reflectivity curves are shown in Fig. 6(a). We observe that the small signal gain is not significantly affected by the pulse duration. However, longer pulse durations decrease the induced TPA losses [Fig. 6(a)] and also increase the gain saturation fluence [Fig. 6(b)]. When we use the input parameters summarized in Table 1 for the 672-fs VECSEL into the RE model, we obtain simulated reflectivity curves which are in good agreement with the measured data points [Fig. 6(a)]. The extracted numerical values for the gain saturation fluence (defined as in [46]) could also be reproduced by the simulation [Fig. 6(b)].

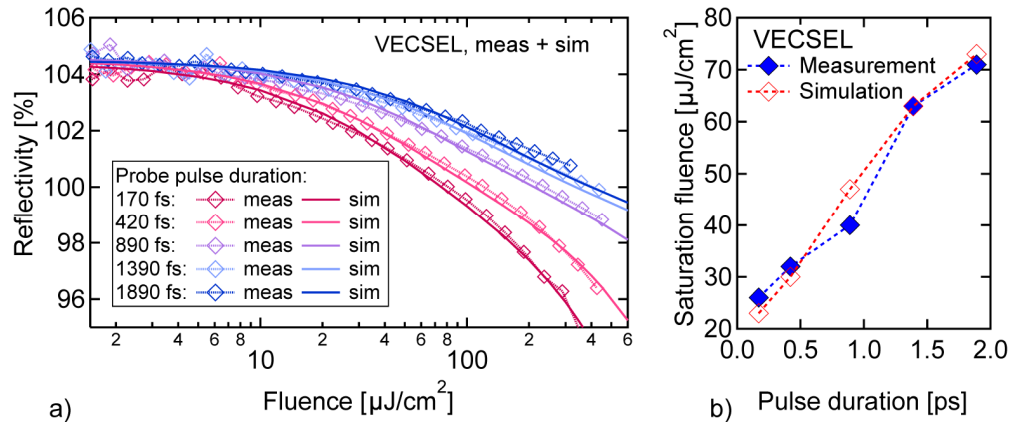


Fig. 6. (a) VECSEL gain saturation measurements. The VECSEL shows an earlier saturation when probed with shorter pulses. (b) Values of measured and simulated gain saturation fluences. The experimental values are obtained through least-square fit of the measured data point to the model described in [46].

The measured behavior is explained as a consequence of spectral hole burning as follows. The incoming pulse stimulates recombination in the QW energetic region covered by the pulse spectrum (N_1 in our model) and burns a spectral hole in the QW population. For low pulse fluence, the spectral hole is shallow and no effect of pulse duration on the small signal gain is observed. On the other hand, as the pulse fluence increases, the spectral hole deepens and is consequently filled via the decay of carriers from the reservoir (N_2). However, if the pulse duration is shorter or comparable to the typical intraband carrier relaxation time τ_{intra} , the hole is not completely refilled during the time the pulse is interacting with the QW. This decreases the carrier density available for the pulse amplification and results in a gain saturation which limits the laser average output power and pulse energy in ultrafast operation.

6. Analysis of the 100-fs VECSEL

In this section, we apply the RE model to fully describe the cavity elements used in the 100-fs VECSEL result reported in [12]. In particular, we obtain quantitative information on the maximum pulse fluence reachable in modelocked operation and on the maximum achievable output coupling (OC) rates. Moreover, we explore the possible advantages of chirped ps-pulses (with subsequent external pulse compression) in terms of output power and efficiency.

Finally, since two different mechanisms (i.e. TPA and gain saturation) are decreasing the effective gain for short pulses, we want to better understand their significance in limiting high-power and efficient ultrafast operation.

6.1 Simulation of the 100-fs VECSEL result

We measured gain saturation for the 100-fs VECSEL under the same experimental conditions that allowed short pulse generation, as reported in [12]. We matched the probing center wavelength to the lasing center wavelength (1034 nm) and applied the same heat-sink temperature (1°C) and pump intensity (21 kW/cm^2). We then fitted the measurement to obtain the correct parameters for the RE model [Fig. 7(a)]. The same was done to reproduce the saturation characteristic of the SESAM used in [12] [Fig. 7(b)]. The SESAM recovery time of 1.5 ps was directly measured in the pump-probe setup. The parameters used in simulations for the 100-fs VECSEL are summarized in Table 1. It is important to emphasize that the model parameters summarized in Table 1 are in the same range for the different SDLs, which is not surprising since all the SDL materials are very similar.

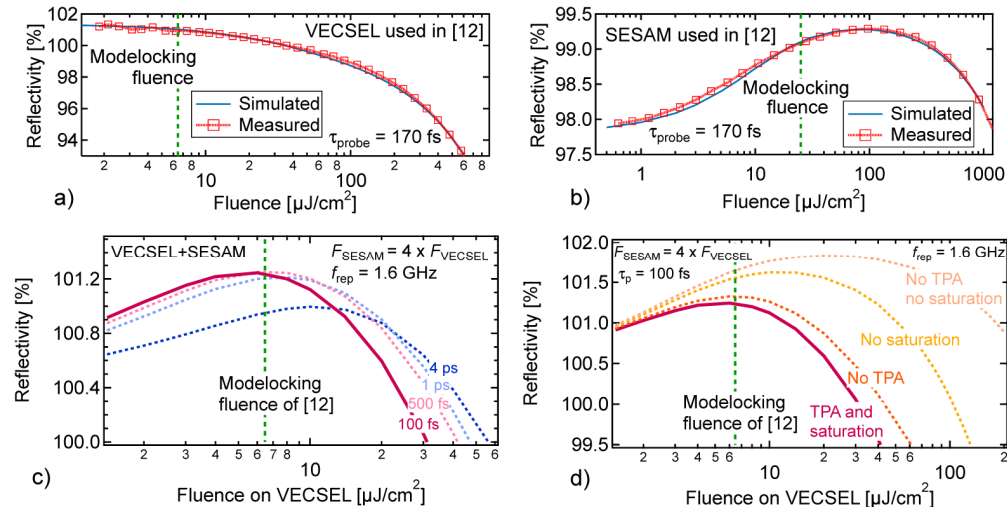


Fig. 7. (a) Fluence-dependent reflectivity for the 100-fs VECSEL chip probed with 170-fs pulses under the same operation conditions described in [12]. The probe pulse is centered at the VECSEL emission wavelength of 1034 nm and has a comparable FWHM spectral bandwidth. The measured saturation behavior is compared to the simulated one. (b) Absorption saturation curve of the SESAM used in [12] and correspondent simulation. (c) Simulation of combined VECSEL and SESAM effects for 100-fs pulses in a V-shaped cavity as described in [12] (solid line). The dashed lines simulate the effects of longer pulses for the same lasing conditions. (d) Simulation of the actual lasing conditions of [12] including gain saturation and TPA (solid line); without TPA in the gain chip (orange dashed line); without gain saturation (yellow dashed line); without TPA and saturation effects in the VECSEL (apricot dashed line).

Using Eq. (7), we reproduced the reflectivity of the 100-fs VECSEL cavity (obtained as the sum of the VECSEL's and SESAM's saturation curves) with a pulse repetition rate of 1.6 GHz and a 100-fs pulse duration as described in [12]. In Fig. 7(c) we observe a cavity reflectivity maximum at a fluence of $F_0 = 6 \mu\text{J}/\text{cm}^2$, which is in good agreement with the actual modelocking fluence of $6.5 \mu\text{J}/\text{cm}^2$. As expected from the model, the laser operates close to the maximum of cavity amplification, where an optimal balance between the effects of unsaturated SESAM, saturated gain and TPA losses occurs.

The quantity F_0 indicates the intracavity pulse fluence that the laser reaches in modelocked operation while the OC rate (defined as $R(F_0) - 100\% - \text{cavity losses}$) sets the power fraction that can be extracted at every roundtrip. Therefore, the combination of the two quantities represents a figure of merit for output power and efficiency of SDLs.

From Fig. 7(c), we extracted $R(F_0) = 101.2\%$ for the 100-fs VECSEL generating 100-fs pulses at 1.6 GHz. In addition, we need to consider $\approx 0.3\%$ of additional fluence-

independent cavity losses mainly introduced by the intracavity Brewster plate, which leads to a total OC rate of 0.9%, in agreement with our previous results [12].

6.2 Simulation of long pulse operation

We simulated the same cavity for 100-fs VECSEL with different pulse durations. We clearly observe that longer pulses shift F_0 to higher fluences [Fig. 7(c)]: for a 4-ps pulse, $F_0 = 12 \mu\text{J}/\text{cm}^2$ which is two times the intracavity pulse energy compared to a 100-fs pulse under the same conditions. This comes at the expense of a reduced OC rate for two reasons:

1. The fast SESAM recovery introduces significant losses for long pulses, increasing the effective absorber saturation fluence. This can be avoided by using a slower saturable absorber.
2. A long pulse extracts carriers more efficiently from the gain QWs. Due to the high repetition rate of the pulse interacting with the gain on the VECSEL (for a V-shaped cavity $\approx 2 f_{\text{rep}}$), the QW cannot be completely refilled in the short interval between two pulses. The stationary population level reached by the QWs after several roundtrips is then reduced together with the gain.

Table 1. Model input parameters for the analyzed SDLs

LASER	300-fs VECSEL [45]	800-fs VECSEL [45]	672-fs VECSEL	100-fs VECSEL [12]	184-fs MIXSEL
τ_c [ns]	1.4	1.4	0.9	1.1	1.1
τ_{intra} [ps]	0.30	0.35	0.37	0.37	0.37
τ_{life} [ps]	140	140	140	140	140
τ_{abs} [ps]	-	-	-	1.5	2.5
Γ_{gain} [ps ⁻¹]	0.07	0.07	0.05	0.03	0.05
Γ_{abs} [ps ⁻¹]	-	-	-	0.2	0.4
g_{ss} [%]	-	-	5.2	2.2	3.0
$\Delta R_{\text{ns,gain}}$ [%]	-	-	0.80	0.85	1.30
ΔR_{abs} [%]	-	-	-	1.7	1.35
$\Delta R_{\text{ns,abs}}$ [%]	-	-	-	0.5	-
F_2, gain [mJ/cm ²]	-	-	9.2	9.2	6.8
F_2, SESAM [mJ/cm ²]	-	-	-	75	-

Table 1. Model input parameters for the analyzed structures. In black, fitted parameters. In red, fixed parameters during fitting procedure. In red bold italic, fixed parameters directly obtained from measurement. For τ_{life} we fixed the value extracted from pump-probe measurement. The gain QWs used in the 672-fs VECSEL, 100-fs VECSEL and the 184-fs MIXSEL were grown under the same conditions in the same MOVPE machine, therefore we fitted τ_{intra} only for the 672-fs VECSEL, keeping the value fixed for successive structures. The embedded QW absorber in the 184-fs MIXSEL is similar to the one in the SESAM used to modelock the 100-fs VECSEL, but we assume that long time annealing during growth slightly increased τ_{abs} . The F_2 values are measured with a probe pulse duration of 170 fs.

In conclusion, the advantages of a chirped pulse formation in SDL cavities, which would in principle allow for a higher F_0 are strongly reduced when a fast saturable absorber is used. In addition, repetition rates below the GHz range cannot be reached without encountering multi pulse instabilities due to the short carrier lifetime in the QW conduction band and also intracavity multi-pass geometries [47, 48] do not reduce the effective repetition rate experienced by the gain chip.

6.3 Effects of gain saturation and TPA

Without modifying the SESAM parameters, we simulated the 100-fs VECSEL cavity for 100-fs pulses removing separately the effects of gain saturation and TPA in the VECSEL chip. As seen in Fig. 7(d), TPA is not playing a dominant role at the low F_0 values we are considering. In contrast, gain saturation is seriously limiting the VECSEL performance: an unsaturable VECSEL could reach an F_0 value twice as high with roughly 1.5 times the OC rate compared to the actual results, meaning 3 times the average output power and pulse energy. The best performances would be clearly achieved in case of absent saturation and TPA, approaching the behavior of solid state lasers, which don't suffer from these limitations [49].

7. Analysis of the 184-fs MIXSEL and optical-to-optical efficiency

7.1 MIXSEL saturation

We measured the fluence-dependent reflectivity for the 184-fs MIXSEL and for the 253-fs MIXSEL described in [15]. Thanks to its monolithic structure including both gain and absorber in the same chip, the MIXSEL offers a direct access to F_0 . We probed the MIXSEL reflectivity at the same lasing conditions (same center wavelength, pump intensity, heat-sink temperature and comparable pulse durations).

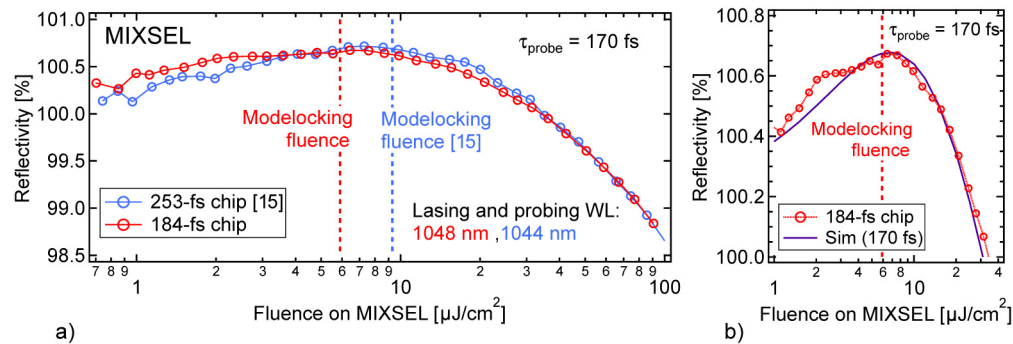


Fig. 8. (a) Measured saturation curve of the 253-fs MIXSEL [15] and of the 184-fs MIXSEL. For both chips, the modelocking fluence almost corresponds to the point of maximum reflectivity. (b) Zoom of the saturation curve of the 184-fs MIXSEL chip and comparison with simulation.

As shown in Fig. 8(a) the measured F_0 values are in good agreement with the experimental modelocking fluences observed for the two lasers, confirming the correlation between F_0 and laser's operation point. We fitted the reflectivity measurements of 184-fs MIXSEL chip [Fig. 8(b)] according to Eq. (6) and extracted the parameters reported in Table 1, which we then use in the following for optical-to-optical efficiency calculations. The maximum OC rate for 184-fs MIXSEL is measured to be 0.68% and F_0 around 7 $\mu\text{J}/\text{cm}^2$, both slightly higher compared to the experimental modelocking values. The low probing repetition rate of 80 MHz allows for maximum refilling of the QWs and therefore a higher F_0 compared to the 4.33-GHz pulse repetition rate, while the cavity losses, principally introduced by the intracavity Brewster plate, reduced T_{OC} to 0.44%. When these effects are taken into account, the model reproduces correctly the actual performance.

7.2 Calculation of optical-to-optical efficiency

We define the optical-to-optical pump efficiency η of the MIXSEL as the ratio between the emitted modelocked power and the incident optical pump power. We used the RE model to numerically reproduce the experimental efficiency value observed for the 184-fs MIXSEL result. Efficiency is a fluence-dependent quantity and hereinafter we will calculate its value at

the laser working fluence F_0 , which in turn varies with the pulse duration and the pulse repetition rate. We determine η_{calc} from:

$$\eta_{calc} = Q_{def} \cdot A_{pump} \cdot \frac{N_{stim}}{N_{stim} + N_{spont}} \cdot \frac{OC(F_0)}{OC(F_0) + \Delta R_{ns,cavity} + \Delta R_{ns} + \Delta R(1 - N_{abs})} \cdot e^{-\frac{F_0}{F_2}} \quad (8)$$

Q_{def} is the ratio between pump and laser wavelengths (quantum defect); A_{pump} is the fraction of the pump power absorbed in the active region (calculated from the design of the semiconductor layer stack with typical values between 0.6 and 0.8); $\Delta R_{ns,cavity}$ represents the intracavity losses, estimated here to be 0.2%; N_{stim} are the carriers recombined via laser stimulation over one roundtrip time T and used for pulse amplification; finally, N_{spont} represents the carriers that spontaneously recombine over T calculated as:

$$N_{spont} = \int_0^T \left(-\frac{N_1(t)}{\tau_{life}} \right) dt \quad (9)$$

We obtain $\eta_{calc} = 0.97\%$ for the 184-fs MIXSEL at a pulse repetition rate of 4.33 GHz, in good agreement with the experimental value $\eta_{meas} = 0.65\%$. Since we do not take into account any recombination process during carrier diffusion in the pumped GaAs and GaAs_{0.94}P_{0.06} barriers, we expected the calculated efficiency to be slightly higher than the real efficiency.

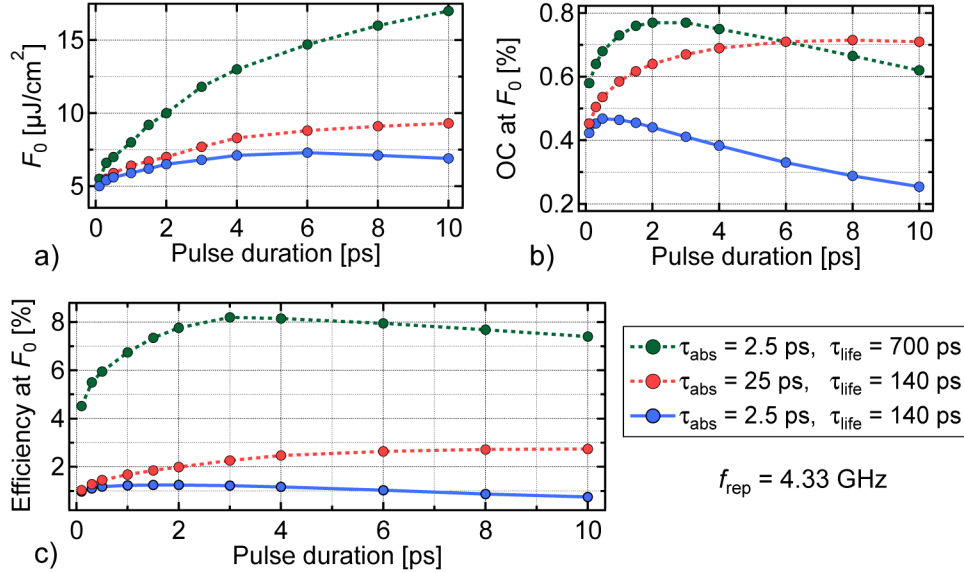


Fig. 9. UltrafastSDL performance with different absorber recovery time and QW gain lifetimes: (a) Calculated F_0 for different pulse durations and MIXSEL parameters. (b) Calculate OC rate at F_0 . (c) Calculated efficiency at F_0 . Solid lines are obtained with the model parameters for the 184-fs MIXSEL (Table 1); dashed lines represent simulation with an increased absorber recovery time or an increased gain QW lifetime.

7.3 Possible solutions to reach higher pump efficiency

Higher pump efficiencies of several percent are reported in [14, 50] for ultrafast SDLs generating picosecond pulses. However, we would like to emphasize that η_{calc} stays below 1.3% for the 184-fs MIXSEL chip when modelocking is simulated for pulse durations up to

10 ps. As discussed for the 100-fs VECSEL, in ps-operation the incomplete QW refilling and the increased absorber losses prevent significant increases in F_0 and OC. This cancels the beneficial effects on the efficiency of the higher gain saturation experimented by long ps-pulses (Fig. 9).

A different behavior is observed when the recovery time of the embedded absorber is increased by a factor of 10, from 2.5 ps to 25 ps. According to [19], sub-300-fs operation cannot be obtained with such a slow saturable absorber but from Fig. 9 we can conclude that η_{calc} would actually be increased to about 3% for 10-ps pulses, which is in agreement with the previously demonstrated better pump efficiency for picosecond MIXSELs.

According to Eq. (9), a short carrier lifetime in the conduction band of the QW gain is the most detrimental parameter for the optical-to-optical pump efficiency. The pulse can interact with the gain medium only for a small fraction of a roundtrip time, while for the remaining time carriers diffuse through the barriers into the QWs and spontaneously recombine before contributing to pulse amplification. We simulated the 184-fs MIXSEL with a τ_{life} five times higher compared to the experimental value, obtaining a significant efficiency increase for all pulse durations, with η_{calc} exceeding 8% for a 3-ps pulse duration.

As indicated in Eq. (9), a shorter roundtrip time reduces the relative efficiency drop caused by spontaneous emission. We simulated modelocked operation for the 184-fs MIXSEL at higher pulse repetition rates of 10 and 30 GHz keeping the pulse duration fixed at 184 fs. In Fig. 10(a) we cannot observe an improvement of F_0 and available OC rate with higher pulse repetition rates. This is consistent with what was measured in [16]: higher repetition rates come at the expense of reduced intracavity pulse fluence and OC rate.

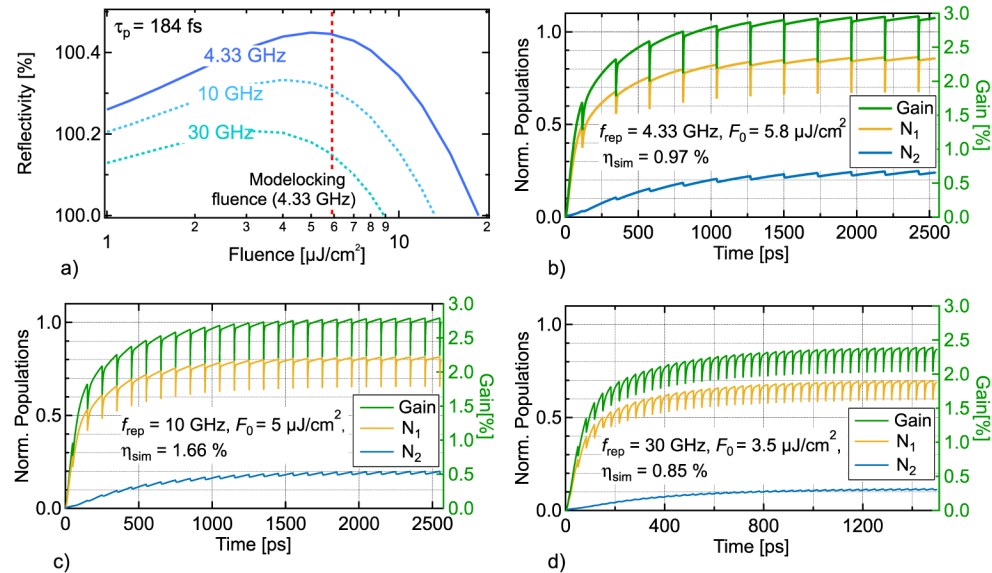


Fig. 10. Ultrafast SDL performance with different pulse repetition rates: (a) MIXSEL saturation curve calculated at different repetition rates. The solid line represents the simulation obtained with the 184-fs MIXSEL parameters at 4.33 GHz; the model reproduces correctly the actual performance; the dashed lines simulate the results for different repetition rates of 10 and 30 GHz; cavity losses are included. (b), (c) and (d): gain and carrier dynamics in the QW gain simulated for different pulse repetition rates. Starting from an initially empty QW, the overall QW population and gain reached at steady-state decrease for reduced roundtrip time. Populations are normalized to the respective maximum values N_{10} and N_{20} .

Compared to the 4.33-GHz result we observe a higher efficiency at 10 GHz ($\eta_{calc} = 1.66\%$), but then a lower efficiency for 30 GHz ($\eta_{calc} = 0.85\%$). This means that reduced gain

for higher pulse repetition rates cancels the potential benefit of the reduced losses of the excited carriers with shorter cavity roundtrip times. One can compare the QW population dynamics in Figs. 10(b)-10(d), simulated at different repetition rates at the respective F_0 . The overall carrier population, and therefore the gain is decreased by the more frequent incoming pulses on the MIXSEL chip.

In conclusion, a longer carrier lifetime in the conduction band is the most promising solution to increase the optical-to-optical pump efficiency for femtosecond SDLs.

8. Conclusion and outlook

In this paper, we have demonstrated a new world-record MIXSEL performance with pulses as short as 184 fs, with an average output power of 115 mW, a pulse repetition rate of 4.33 GHz and a center wavelength of 1048 nm. This corresponds to a peak power of 127 W. The MIXSEL chip has 10 InGaAs QWs for the gain and one single InGaAs QW for the saturable absorber. We used a simple linear cavity with an output coupler transmission of 0.44% and an intracavity Brewster plate to obtain linear polarization. This new result was obtained with a pump efficiency of only 0.65% and unfortunately confirms the trade-off in output power and optical-to-optical pump efficiency with shorter pulses.

To explain in more details the physical reasons for this trade-off, we employed and justified a rate equation (RE) model describing the InGaAs QWs normally used as active medium. By making careful approximations it was possible to make the model parameters accessible through direct measurements or fits of available experimental data. Despite its simplicity compared to other QW laser dynamical models, our model succeeds to accurately reproduce the experimental gain saturation curves obtained by probing the reflectivity of a pumped VECSEL at different pulse durations and correctly describes the output power and the pump efficiency for several different ultrafast SDL results based on SESAM modellocked VECSELS and MIXSELS. For shorter pulses, spectral hole burning decreases the carrier density available for the pulse amplification and therefore increases gain saturation effects and lowers the output power.

With the intent of analyzing the behavior of a full SDL cavity, we measured and fitted the VECSEL and the SESAM used for the 100-fs pulse generation presented in [12]. We concluded that the operation point of a modellocked SDL is set by the macroscopic fluence parameter F_0 , where the cavity round-trip pulse amplification is maximized. We can conclude that gain saturation in general and not TPA in the VECSEL chip is the dominant process that limits F_0 , the output coupling rate and therefore the output power.

The saturation characteristic was also measured and fitted for the 184-fs MIXSEL and confirmed our understanding from the ultrafast VECSEL analysis. Furthermore, a more detailed study on optical-to-optical pump efficiency was carried out searching for possible improvements. Long picosecond pulses are less affected by spectral hole burning but can achieve higher efficiencies only if the absorber recovery is kept slow (in the tens of picosecond). Higher repetition rates can in principle benefit from higher frequent and efficient amplification in the gain chip, but they do not offer improved efficiency performances because of the incomplete carrier refilling of the QWs between two consecutive pulses. We found that the main efficiency limitation is given by the short carrier lifetime in the conduction band of our QWs (measured to be approximately 140 ps). This low carrier lifetime is typical for high-power ultrafast SDLs with a typical output coupler of less than 1%.

From this analysis we can conclude that the main parameter that needs to be optimized for more efficient femtosecond SDLs is the carrier lifetime. We believe that significant improvements can be achieved with quantum dot (QD) instead of QW gain materials.

Funding

Swiss Confederation Program Nano-Tera.ch, which was scientifically evaluated by the Swiss National Science Foundation (SNSF).

Acknowledgments

The authors acknowledge support of the technology and cleanroom facility FIRST for advanced micro-and nanotechnology.